Short- and long-term effects of GPS measured crustal deformation rates along the south central Andes

Giorgi Khazaradze[1] and Jürgen Klotz

GeoForschungsZentrum Potsdam, Kinematics/Neotectonics, Potsdam, Germany

[1] In this study we present the contemporary crustal deformation field along the central and southern Andes (17−42°S) estimated from four Global Positioning System (GPS) campaigns conducted in 1994−1997. We find that the majority of the observed crustal deformation field is relatively homogenous: roughly parallel to the plate convergence direction with decreasing velocities away from the trench. We attribute this type of deformation pattern to the interseismic phase of an earthquake deformation cycle caused by 100% locking of the thrust interface between the subducting Nazca and the overriding South American plates. We have also detected a strong postseismic deformation signal in the vicinity of the 1995 M_w8.0 Antofagasta (22−26°S) and 1960 M_w9.5 Chile (38−43°S) earthquakes. This type of deformation can be described as short-term in nature compared to geological timescales. The above conclusions are based on the results of the three-dimensional (3-D) Andean Elastic Dislocation Model (AEDM). By subtracting the AEDM-predicted deformation rates from the observations we obtained a residual velocity field that highlights the postseismic as well as more long-term deformation effects. For example, we find strong evidence for the continuing crustal shortening across the back arc, reaching its maximum (4 mm/yr) in the very north of our study area. In addition, between latitudes 29°S and 34°S, there is an indication of E-W oriented extension within the forearc, in accordance with the recent geologic findings for the N-S oriented normal faulting. *INDEX TERMS:* 1243 Geodesy and Gravity: Space geodetic surveys; 1206 Geodesy and Gravity: Crustal movements—interplate (8155); 7215 Seismology: Earthquake parameters; 8102 Tectonophysics: Continental contractional orogenic belts; *KEYWORDS:* Andes, GPS, earthquake cycle, crustal deformation, subduction, back-arc shortening

1. Introduction

[2] The estimation of contemporary crustal deformation rates along active continental margins plays an important role in understanding the kinematics and dynamics of physical processes taking place in these complex tectonic environments. This is especially true for subduction zones, where the oceanic plate thrusts beneath the continent, causing the overriding plate to deform dramatically. However, until the introduction of the Global Positioning System (GPS) technology for scientific applications a little more than a decade ago, the acquisition of dense and highly precise measurements of such deformation was not possible.

[3] The primary objective of our work presented in this paper is to determine the nature of contemporary crustal deformation along the south central Andes and to link these observations with the tectonic processes driving lithosphere deformation along this active convergent plate margin. Specific questions that we attempt to answer include: What is the magnitude and orientation of crustal deformation rates along the south central Andes? What are the main driving forces behind the observed deformation? What part of the observed signal can be attributed to long-term, geologic deformation processes?

2. Tectonic Setting

[4] Andean subduction zone (ASZ) represents the longest convergent margin in the world, stretching for more than 7000 km along the western coast of the South American continent, from Colombia to southern Chile (Figure 1). As a result of continuing subduction of the oceanic Nazca and Antarctic plates beneath the continental South American plate, the ASZ has developed an extensive orogenic belt.

[5] The ASZ is characterized by the presence of distinct tectonic structures paralleling the strike of the trench. These include (listed from west to east): (1) The forearc region between the 3−8 km deep Chile trench and the volcanic arc,

---

[1]Now at Departament de Geodinàmica i Geofisica, Universitat de Barcelona, Barcelona, Spain.
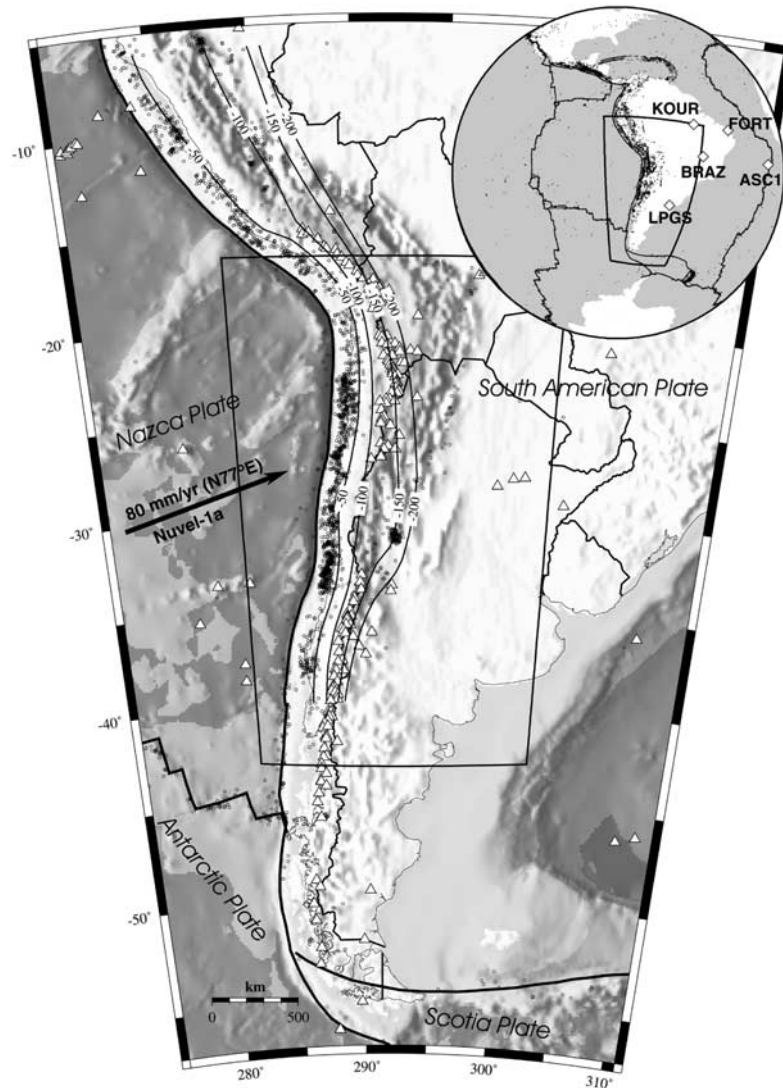
Figure 1. Tectonic setting of the study area (shown as a box). Solid dots represent the distribution of shallow seismicity (<70 km depth) since 1964 based on relocated ISC hypocenter data [*Engdahl et al.*, 1998]; Black contour lines show the depth of the subducting slab [*Cahill and Isacks*, 1992; *Creager et al.*, 1995]. Quaternary volcanoes are depicted as triangles [*Simkin and Siebert*, 1994]; Bathymetric and topographic data are based on the work by *Smith and Sandwell* [1997]. Diamonds inside the inset show IGS GPS stations used in defining the stable South American continent.

represented by the Coastal Cordillera, Longitudinal Valley, North Chilean Precordillera and the Preandean depression; (2) the magmatic arc represented by Principal and Frontal Cordilleras (also referred to as Western Cordilleras), consisting of Miocene-Quaternary volcanic cones, often exceeding 5000 m in elevation (shown as open triangles in Figure 1); and (3) the back arc, located between the magmatic arc and the stable part of South American continent. Bounded by the Western and Eastern Cordilleras is the Altiplano-Puna plateau with elevations ranging between 3800 and 4500 m and with a longitudinal extent reaching 400 km. To the east the plateau is flanked by the Eastern Cordillera and the Sierras Subandeanas. The latter is a typical thin-skinned fold and thrust belt [*Jordan et al.*, 1983]. Most of the crustal shortening (up to 230 km since the Neogene time) took place in the Eastern Cordillera and

the Subandean zone [*Kley and Monaldi*, 1998]. The Chaco foreland, between the Subandean zone and the Brazilian Craton, represents an active back-arc basin, filled with continental sediments.

[6] In addition to the above mentioned trench parallel features, Andean tectonics is also characterized by prominent along-strike variations [e.g., *Jordan et al.*, 1983], which are most often related to the changing geometry of the subducting Nazca plate [*Cahill and Isacks*, 1992; *Creager et al.*, 1995]. As can be seen from Figure 1, between 100 and 200 km depth the dip angle of the slab varies significantly, producing two relatively flat sections. For some time it has been recognized that the Cenozoic magmatic centers are mostly found above the steep portions of the slab [*Cahill and Isacks*, 1992; *Whitman et al.*, 1996], while shallow seismicity (<70 km) is more concentrated

above the flat portions [*Jordan et al.*, 1983; *Gutscher et al.*, 2000]. In addition, the level of seismicity in the forearc is considerably higher than in the back arc. However, south of 33°S latitude, the forearc seismicity decreases significantly, which spatially correlates with the steepening of the subducting slab [e.g., *Gutscher et al.*, 2000].

3. Present-Day Velocities

3.1. GPS Network and Observations

[7] The GeoForschungsZentrum (GFZ) launched the South American Geodynamic Activities (SAGA) project in 1993 as a cooperative effort with numerous organizations and institutions in Argentina and Chile, with the main objective of studying the kinematics and dynamics of present-day deformation processes along the central and southern Andes. Currently the SAGA network consists of 230 geodetic markers spanning more than 4000 km from the Peru/Chile border in the north to Cape Horn in the south. After the first few years of observations it became clear that the contemporary surface deformation along the central Andean forearc is dominated by transient effects related to large thrust type earthquakes. The latter occur at the interface between the subducting Nazca and the overriding South American plates. The majority of the observed crustal deformation field can be explained by the elastic strain accumulation during the interseismic phase of the earthquake deformation cycle [*Klotz et al.*, 2001]. In addition, at the initial phase of our observations, we were fortunate to capture the coseismic displacements associated with the 1995 M_w8.0 Antofagasta earthquake [*Klotz et al.*, 1999].

[8] The results presented here (Figure 2) are derived from 112 GPS sites observed during the four GPS campaigns conducted between 1994 and 1997 (Table 1). The velocities from the central and the southern parts of the study area are based on the 1994–1996 campaigns and were presented earlier by *Klotz et al.* [2001]. The velocities for the northern part of the network between latitudes 17°S and 22°S that were deduced from 1996 to 1997 occupations, are published here for the first time (Figure 3 and Table 2). These data fill the gap between the earlier reported results in the north [*Norabuena et al.*, 1998; *Bevis et al.*, 1999; *Kendrick et al.*, 2001] and the south [*Klotz et al.*, 2001].

[9] Each site was observed for at least three consecutive days with daily observation periods exceeding 20 hours. Throughout the various observations we used a common monumentation procedure, which allows a direct connection of the antenna with the marker. This way an accurate relocation of the antenna over the individual geodetic marker during repeated observations is ensured, minimizing the eccentricity errors. Site coordinates and velocities were derived in three steps using the GFZ processing software EPOS (Earth Parameter and Orbit System) that uses undifferenced phase and pseudorange observables [*Angermann et al.*, 1997]. In the first step, fiducial-free station coordinates were obtained by combined analysis of the data from the campaign and permanent IGS sites. Satellite orbits and clocks were held fixed using IGS combined satellite orbits and Earth orientation parameters [*Beutler et al.*, 1999]. In the second step, the fiducial-free solution was transformed to global International Terrestrial Reference Frame (ITRF97) [*Sillard et al.*, 1998]. At the final third

step this solution was transformed to a fixed South America reference frame, by estimating a best fitting Euler vector for the South American plate using a least squares adjustment approach and the ITRF97 velocities for five IGS stations located on a stable part of the South American continent, shown in the inset of Figure 1. The mean value of position residuals for these stations, that reflect the achieved regional network precision, ranges between 2–4 mm and 5–7 mm for horizontal and vertical components, respectively. Considering the given vertical precision and the fact that the expected rates of surface uplift in the ASZ do not exceed 2 mm/yr, two observations separated by 1 or 2 years are not sufficient to resolve the possible vertical motions with adequate confidence. Hence, in this study we only consider the horizontal components of deformation.

3.2. Crustal Deformation Rates

[10] The main result of this study is shown in Figure 2 as velocity vectors, representing the contemporary crustal deformation field along the south central section of the Andean convergent margin. It is evident that most of the observed points are moving in a uniform and consistent fashion: parallel to the plate convergence direction and with velocities decreasing away from the deformation front. This type of deformation can be explained by the interseismic phase of earthquake deformation cycle, caused by the locking of the thrust interface between Nazca and South American plates. However, the two areas located within the northern and southern parts of the study area are clearly exhibiting a different type of deformation. In the northern area, highly nonuniform distribution of velocity vectors is due to the postseismic effects of the 1995 M_w8.0 Antofagasta earthquake. For that reason, the vectors derived from the 1995–1996 and 1996–1997 campaigns differ significantly from one another (Figure 4). From these vectors it is evident that while the postseismic effects dominate the velocity field in the first year after the occurrence of the event, in the second year the interseismic deformation becomes dominant. Detailed studies of temporal-spatial evolution of the deformation field in the region is underway and will be a subject of a forthcoming paper. In the southern section, although the derived deformation field is less chaotic, the close examination of the velocity vectors reveals an anomalous trenchward directed motion of the stations located south of 38°S and farther inland. We explain these motions, with the aid of 3-D viscoelastic finite element model, in terms of continuing postseismic crustal deformation due to mantle stress relaxation in response to the 1960 M_w9.5 Chile earthquake [*Khazaradze et al.*, 2002].

3.3. Strain Rate Calculation

[11] One of the main advantages of using GPS technology for deformation measurements, as opposed to terrestrial geodetic techniques, is the ability to determine absolute displacement vectors, including rigid-body motions (rotations and translations), as well as internal deformation (strains) [*Dixon*, 1991]. While the former is useful to study long-term deformation processes, the latter is more applicable for studying the short-term, transient deformation effects associated with various phases of the earthquake cycle [*Khazaradze*, 1999].
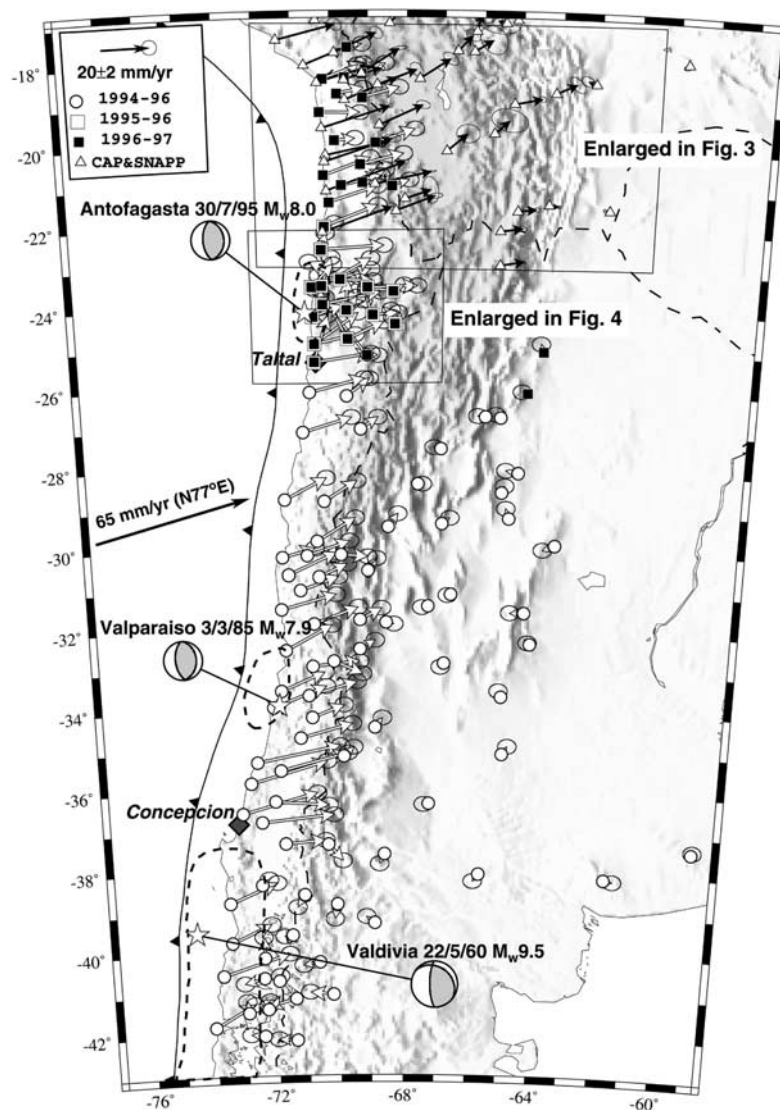
Figure 2. Velocity vectors of SAGA GPS network relative to the stable South American continent. The results are based on 1994–1996 (open circles), 1995–1996 (open squares), 1996–1997 (solid squares) occupations. In the northern part of the network we also display the results of *Kendrick et al.* [2001] (open triangles), who have integrated the previously published data from CAP [*Bevis et al.*, 1999] and SNAPP [*Norabuena et al.*, 1998] GPS networks. Stars with surrounding dashed lines show the epicenters and the aftershock distribution areas for 1960 M_w9.5 Chile [*Plafker and Savage*, 1970; *Cifuentes*, 1989], 1985 M_w7.9 Valparaiso [*Barrientos*, 1988] and 1995 M_w8.0 Antofagasta [*Ruegg et al.*, 1996] earthquakes. Nazca/South American plate convergence vector is based on the estimate of *Angermann et al.* [1999]. Shading represents 30-arc sec topography archived by the USGS (http://edcdaac.usgs.gov/gtopo30/gtopo30.html).

[12] To examine the variability in the observed deformation field, we have subdivided the study area into 10 roughly square shaped zones with approximately 300 km long sides (Figure 5). Seven of these zones (1, 2, 3, 4, 6, 8, and 10) are located within the forearc, and three of them (5, 7, and 9) cover the back-arc region. For each of the zones, we calculated the principal horizontal strain rate and rigid-body motion parameters assuming a uniform strain distribution within the zone. Two main characteristics of the calculated strain field (Figure 5 and Table 3) are (1) an order of magnitude lower deformation rates in the back arc compared to the forearc and (2) purely uniaxial E-W

oriented contraction in the forearc. The more clockwise orientation of $\dot{\varepsilon}_2$ (Θ in Table 3) as compared to the velocity vectors (Figure 2) and the plate convergence direction (D in Table 3) indicates the presence of trench-parallel rigid-body

Table 1. Occupation History of SAGA Campaigns

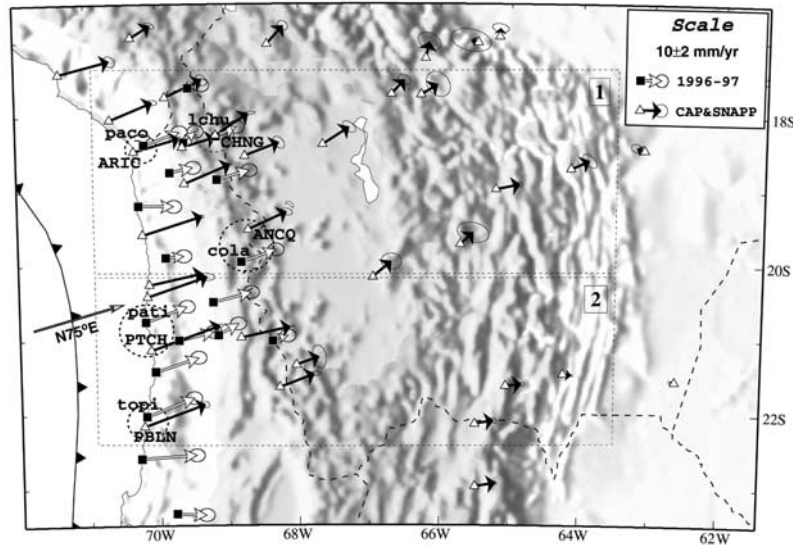| Years	Number of Stations	Zone	Source
1994–1996	80	23–45°S	*Klotz et al.* [2001]
1995–1996	16	22–26°S	*Klotz et al.* [2001]
1996–1997	33	17–26°S	Table 2

Figure 3. Enlarged view of the northern part of the study area from Figure 2. Five selected pairs of SAGA and CAP/SNAPP stations, shown with dashed circles and identified with four-letter station names, were used to estimate the average discrepancy between the two data sets.

translations. Similar type deformation was suggested by *Wang et al.* [2001] for the Cascadia subduction zone. It is also noteworthy that the rigid-body translation rates (C in Table 3) for the zones located within the forearc are high (12–25 mm/yr) and are all roughly parallel to the plate convergence direction. We attribute this observation to the effects of plate locking. As it will be shown in section 4, after subtraction of subduction related effects, the translation rates are significantly reduced. Another important observation that can be seen in the calculated principal

Table 2. SAGA Station Velocities Relative to Stable South America Based on the 1996–1997 Campaigns[a]

No.	Station ID	Longitude	Latitude	W-E Velocity, mm/yr ± 1σ	S-N Velocity, mm/yr ± 1σ	Correlaltion Coefficients
1	BAQU	290.219	−23.342	13.9 ± 3.5	−0.6 ± 2.8	0.03
2	CALC	289.468	−24.264	12.6 ± 3.7	4.6 ± 2.9	0.06
3	CAMA	289.729	−19.206	16.8 ± 3.3	−0.3 ± 2.9	−0.01
4	CARI	289.501	−24.947	17.0 ± 3.0	3.9 ± 2.8	0.03
5	CECU	295.365	−26.138	−2.2 ± 3.0	0.5 ± 2.8	0.05
6	COBA	290.411	−24.824	15.0 ± 3.2	7.2 ± 2.8	0.04
7	COLA	291.181	−19.965	16.5 ± 3.0	5.7 ± 2.9	0.01
8	COME	290.111	−19.908	8.5 ± 3.0	0.9 ± 2.9	−0.01
9	ESIM	291.102	−24.226	10.5 ± 3.0	0.9 ± 2.8	0.04
10	GUAT	290.848	−20.944	9.4 ± 3.0	5.3 ± 2.9	0.01
11	JULO	289.454	−23.526	8.9 ± 3.5	9.3 ± 2.8	0.03
12	LCHU	290.839	−18.275	9.8 ± 3.0	4.4 ± 3.0	−0.01
13	LHER	290.940	−25.223	4.6 ± 3.1	−0.1 ± 2.8	0.04
14	LIVE	289.747	−23.964	23.9 ± 3.0	5.0 ± 2.8	0.02
15	MINF	290.394	−24.105	4.4 ± 3.0	5.5 ± 2.8	0.03
16	OFLA	290.284	−21.018	16.4 ± 2.9	4.1 ± 2.9	0.00
17	OLLE	295.772	−25.102	−1.2 ± 3.0	3.3 ± 2.8	0.06
18	PACO	289.817	−18.391	17.1 ± 3.0	6.2 ± 3.0	−0.02
19	PAEL	290.959	−23.538	20.6 ± 2.9	0.6 ± 2.8	0.03
20	PASO	291.709	−24.449	−1.1 ± 2.9	2.7 ± 2.8	0.03
21	PATI	289.810	−20.768	19.6 ± 2.9	7.3 ± 2.9	−0.01
22	PCHA	290.179	−18.760	11.1 ± 3.0	2.3 ± 2.8	0.01
23	PCUA	289.724	−22.602	25.9 ± 2.9	1.6 ± 2.8	0.01
24	PENI	291.654	−23.640	4.6 ± 3.0	2.7 ± 2.8	0.03
25	PICA	290.777	−20.503	18.0 ± 3.0	4.6 ± 2.8	0.01
26	PUQI	291.622	−21.026	7.2 ± 3.2	2.4 ± 2.9	0.03
27	RLOA	289.944	−21.434	20.3 ± 2.9	6.6 ± 2.8	0.00
28	SURI	290.846	−18.858	15.4 ± 3.1	4.3 ± 3.0	0.00
29	TALT	289.490	−25.400	23.5 ± 3.0	3.6 ± 2.8	0.03
30	TOPI	289.806	−22.034	22.4 ± 3.0	8.7 ± 2.8	0.01
31	URIB	289.720	−23.505	20.5 ± 3.0	11.3 ± 2.8	0.02
32	VIRI	290.452	−17.624	6.3 ± 3.0	1.3 ± 3.0	−0.01
33	ZAHU	290.380	−18.357	5.8 ± 3.0	5.2 ± 3.0	−0.01

[a]Tables for 1994–1996 and 1995–1996 are given by *Klotz et al.* [2001].
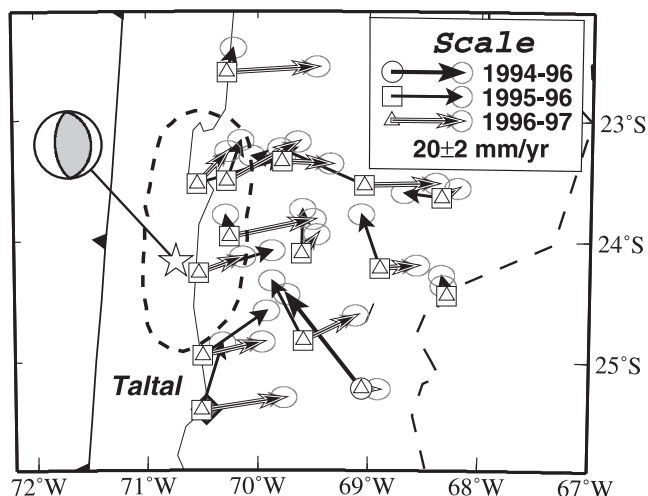
Figure 4. Temporal variations in the postseismic deformation following the 1995 Antofagasta earthquake. Dashed line outlines the aftershock distribution area of the event [*Ruegg et al.*, 1996].

strain field is an abrupt increase in estimated strain rates between the two northern zones: from almost no strain in the northernmost zone to −0.08 μstrain/yr in zone 2. This is caused by a considerably more gradual landward decrease in the observed velocities for the stations located in zone 1. In other words, the deformation in the northernmost part of our study area is transmitted farther inland. Causes and consequences of these observation will be discussed in section 5.2.

4. Andean Elastic Dislocation Model

4.1. Introduction

[13]   In order to properly interpret the tectonic significance of observed velocities, we constructed a three-dimensional model of the seismogenic interface between the subducting Nazca and the overriding South American plates and used elastic dislocation theory to predict the amount of interseismic deformation at a given set of observation points. We will refer to this model as an Andean Elastic Dislocation Model (AEDM).

[14]   The two main parameters that we intend to estimate through our modeling efforts are the width of the seismogenic zone and the amount of coupling along the subduction thrust interface. The width of the seismogenic zone is defined by its updip and downdip depth limits. At the updip limit of the seismogenic zone the mechanical behavior of the fault changes from stable sliding to stick-slip, driven by the transformation of smectite-rich clays to illite and chlorite due to increased temperature (100–150°C) at the plate interface [e.g., *Hyndman et al.*, 1997]. For the purpose of our studies, the exact location of the updip limit is not very important, since the deformation rates observed onshore are not sensitive to this parameter. The downdip limit of the seismogenic zone is normally described by the depth extent of the locked and transition zones, characterized respectively, by stick-slip and brittle behavior. According to *Hyndman and Wang* [1993], earthquakes can nucleate only within the locked zone, while the rupture may propagate

deeper into the transition zone [see also *Oleskevich et al.*, 1999]. *Hyndman and Wang* [1993] suggest that the boundary between these two zones is governed by the thermal effects and coincides with 350°C isotherm. In case of subduction of old (i.e., cold) oceanic crust, 350°C temperature on the thrust interface is usually reached below 100 km depth, much deeper than 50–60 km depth limit for the occurrence of thrust type earthquakes [*Pacheco et al.*, 1993; *Tichelaar and Ruff*, 1993]. Therefore, in this case the
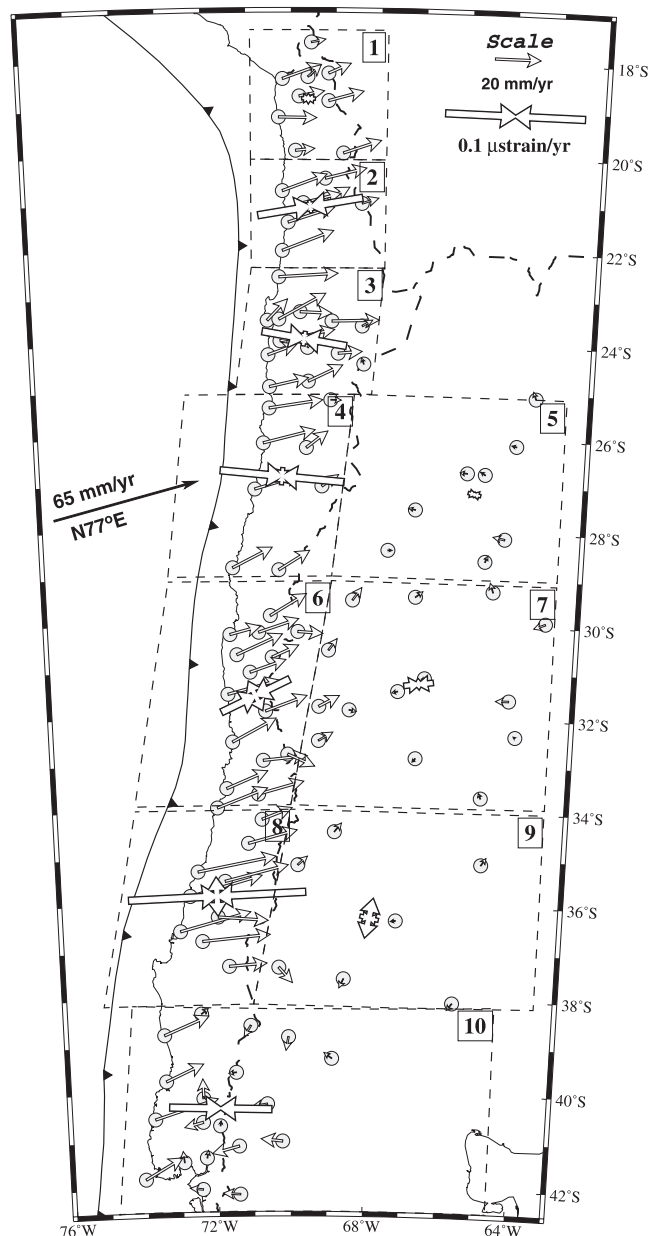

Figure 5. Horizontal strain rates for the SAGA network based on GPS velocities estimated from the 1994–1996 and 1996–1997 campaigns. Strain crosses are located at the center of mass of individual subregions and represent minimum ($\dot{\varepsilon}_1$) and maximum ($\dot{\varepsilon}_2$) principal strain rates. Zones 3 and 10 cover areas affected by the 1995 Antofagasta and 1960 Chile earthquakes, respectively. Numerical results are given in Table 3.

Table 3. Horizontal Strain, Rotation, and Translation Rates From 1994–1996 and 1996–1997 Data for the Regions Shown in Figure 5

No.	$\dot{\varepsilon}_1{}^a \pm 1\sigma$	$\dot{\varepsilon}_2{}^b \pm 1\sigma$	$\Theta^c \pm 1\sigma$	$\Omega^d \pm 1\sigma$	$C^e \pm 1\sigma$	$C\alpha^f \pm 1\sigma$	D^g
1	0.004 ± 0.046	−0.008 ± 0.052	90 ± 28	−1.3 ± 0.3	12.3 ± 0.6	74 ± 3	75°
2	−0.007 ± 0.060	−0.075 ± 0.057	80 ± 7	0.7 ± 0.4	17.1 ± 0.7	71 ± 2	75°
3*	−0.009 ± 0.030	−0.060 ± 0.030	100 ± 4	1.7 ± 0.2	14.6 ± 0.5	73 ± 2	75°
4	−0.011 ± 0.024	−0.089 ± 0.028	95 ± 2	0.8 ± 0.2	16.2 ± 0.5	69 ± 2	76°
5	−0.002 ± 0.019	−0.008 ± 0.020	103 ± 26	−0.3 ± 0.2	2.3 ± 0.5	121 ± 13	73°
6	0.021 ± 0.012	−0.054 ± 0.016	64 ± 2	1.3 ± 0.2	17.4 ± 0.3	73 ± 1	76°
7	0.006 ± 0.009	−0.020 ± 0.008	82 ± 3	0.2 ± 0.1	1.8 ± 0.3	22 ± 10	74°
8	0.026 ± 0.030	−0.127 ± 0.034	88 ± 1	1.9 ± 0.2	25.6 ± 0.4	79 ± 1	77°
9	0.027 ± 0.013	−0.012 ± 0.012	102 ± 3	0.1 ± 0.1	1.4 ± 0.5	108 ± 20	75°
10[h]	−0.000 ± 0.011	−0.073 ± 0.012	92 ± 1	1.7 ± 0.1	2.6 ± 0.3	33 ± 7	77°

[a]Minimum (least compressive) principal strain rate in μstrain/yr.
[b]Maximum (most compressive) principal strain rate in μstrain/yr.
[c]Azimuth of $\dot{\varepsilon}_2$ measured clockwise from north.
[d]Rigid body rotation in °/Myr (positive is clockwise.)
[e]Rigid body translation in mm/yr.
[f]Translation azimuth in degrees from north.
[g]Plate convergence azimuth measured clockwise from north [*Angermann et al.*, 1999].
[h]Zones affected by 1995 M_w8.0 Antofagasta and 1960 M_w9.5 Chile earthquakes.

controlling factor of the extent of seismic coupling is the depth of interaction between the downgoing slab and the mantle wedge, which is encountered at the depth ranges between 35 to 50 km, corresponding to an average depth of the forearc continental Moho [e.g., *Oleskevich et al.*, 1999].

4.2. Model Constraints

[15] With the aim of minimizing the number of unknown input parameters, the shape of the upper surface of the subducting Nazca plate (i.e., slab geometry) and Nazca/South America convergence direction and rate were constrained from independent geophysical observations.

[16] To constrain the geometry of the subducting Nazca plate, we estimated the location and the depth of the deformation front (i.e., trench) from ocean floor bathymetry [*Smith and Sandwell*, 1997] and connected it with slab isodepth contours estimated by *Cahill and Isacks* [1992] and *Creager et al.* [1995] based on the distribution of Wadati-Benioff zone earthquakes. For the purpose of dislocation modeling the exact geometry of the slab below 60–70 km depth is not very important, since the seismogenic zone of the thrust interface probably does not extend below this depth.

[17] The plate convergence parameters used in our modeling were derived based on the Nazca/SA Euler pole estimated by *Angermann et al.* [1999] and located at latitude 48.8°N and longitude 91.7°W with an angular velocity of 0.59°/Myr. This corresponds to the plate convergence rate of 65 mm/yr in the direction of N77°E at latitude 30°S. This rate is approximately 20% lower than the rate predicted by the NUVEL-1A global plate motions model [*DeMets et al.*, 1990, 1994]. As suggested previously by *Norabuena et al.* [1999], this discrepancy is most likely caused by a diminished plate convergence rate in the past 3 Myr.

4.3. Model Description

[18] The model calculations were performed using a modified version of the DISL3D program, initially developed by *Flück et al.* [1997]. The main principle of the model is based on *Okada*'s [1992] formulation for dislocations in a homogenous elastic half-space due to a point source force. At the initial step the fault surface is divided into numerous triangular elements, each with an area of ∼1 km² to approximate the point source. Consequently, the contributions of individual triangular elements are summed
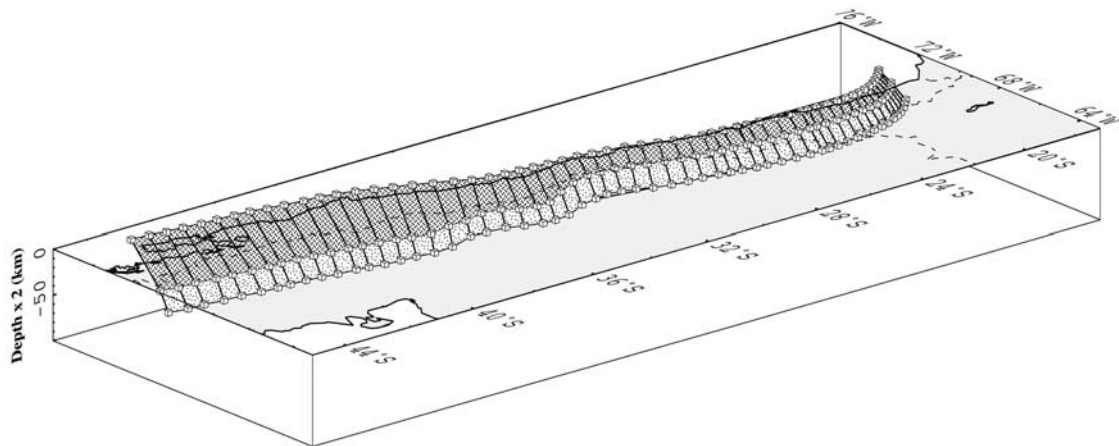

Figure 6. Three-dimensional view of the Andean Elastic Dislocation Model (AEDM). In the northern section the alternative model is displayed (denoted as North2 in Table 4 and shown with dotted lines in Figure 7). Vertical exaggeration of 2. See Figure 7 caption for more details.
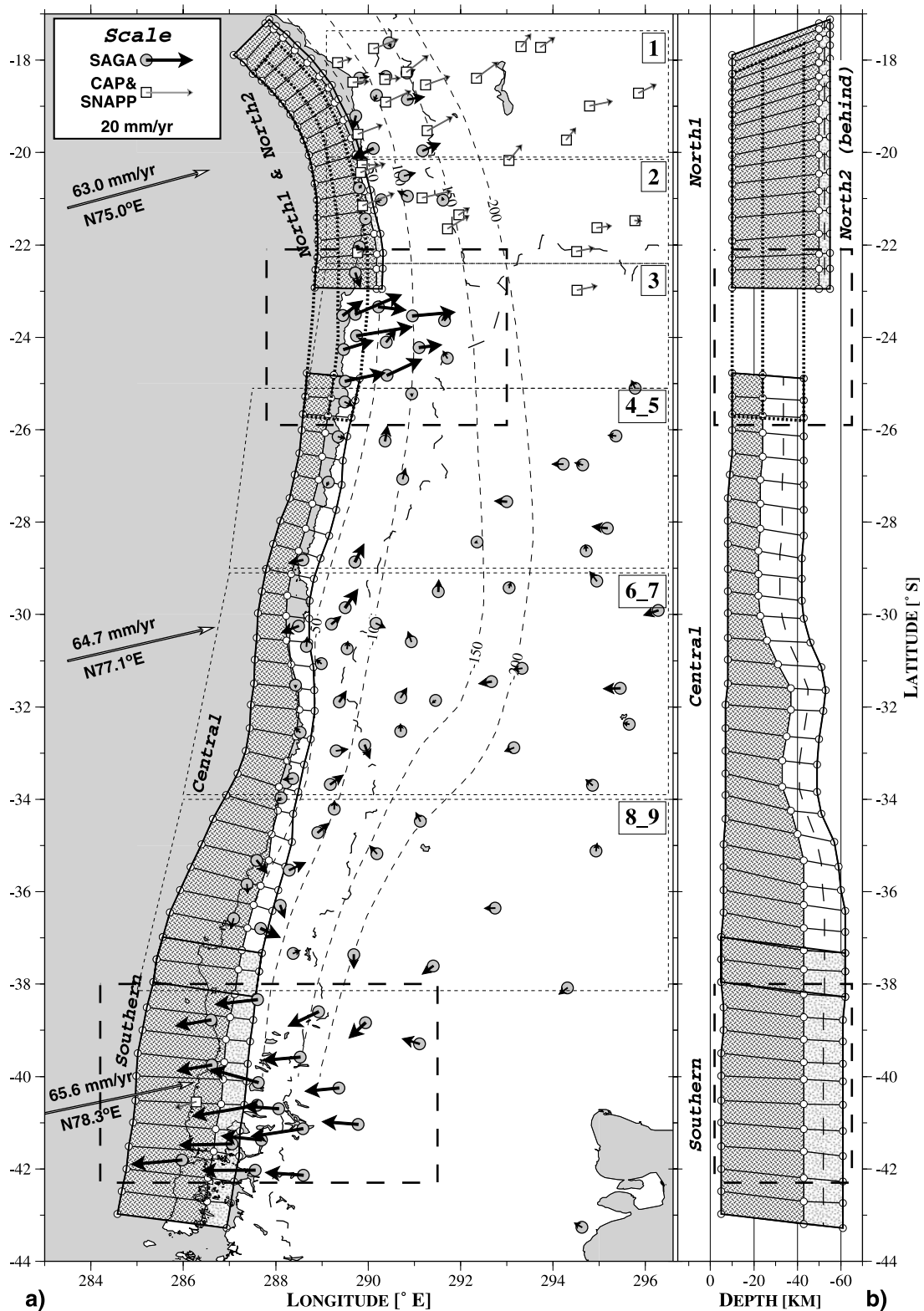
Figure 7. Seismogenic zone along the Nazca/South America thrust interface deduced from the AEDM. For the northern section behind the preferred model (North1 in Table 4) the alternative (North2 in Table 4) model with shallower seismogenic zone is displayed using dotted lines. Locked and the transition zones are shown as dark and light shaded regions, respectively. The outlines of the three overlapping segments of the model are shown with thick lines. Two rectangles represent the postseismically affected regions. See Figure 2 caption for further information. (a) Vectors depict residual velocities obtained by subtracting the interseismic signal predicted by the AEDM from the observed velocities. (b) North-south cross section of the seismogenic zone. The dashed line in the middle of the transition zone shows the average depth extent of geodetically estimated seismic coupling.

Table 4. AEDM Parameters

Segments	L^a	N^b	T^c	S^d	D^e
North1	650	54	95200	63.0	75.0°
North2[f]	900	22	117600	63.0	75.0°
Central	1400	84	151200	64.7	77.1°
Southern	650	39	67200	65.6	78.3°

[a]N-S length of the model segment in km.
[b]Number of nodal points in the initial grid.
[c]Total number of triangular elements.
[d]Plate convergence rate in mm/yr.
[e]Plate convergence azimuth measured clockwise from north.
[f]An alternative model shown with a dotted line in Figure 7.

up using numerical integration technique. Such an approach enables us to account for the existing along strike variations in the geometry of the subducting Nazca plate (Figure 6). To simplify the modeling procedure the fault interface along the entire length of the study area is subdivided into three overlapping sections: northern, central, and southern, as outlined with solid black lines in Figure 7. Each of these sections is modeled separately, taking into account slight variations in the plate convergence parameters, as predicted by the location of the Euler pole calculated by *Angermann et al.* [1999] (Table 4 and Figure 7):

$$L_1 = \frac{1}{N} \sum_{i=0}^{N} \frac{|\text{Data} - \text{Model}|}{\sigma_i} \qquad (1)$$

$$L_2 = \frac{1}{N} \sum_{i=0}^{N} \left(\frac{\text{Data} - \text{Model}}{\sigma_i} \right)^2 \qquad (2)$$

In the starting model the downdip limits of the locked and transition zones were initially constrained to 30 and 45 km depths, respectively. Consequently, these depths were varied through forward modeling to achieve the best fit for every station in question. Greater weight was given to models that matched the observations at coastal stations, where the observed velocities are at their maximum. The preferred model was selected from more than 3 dozen runs by minimizing the L_1 and L_2 norms calculated using equations (1) and (2). Specifically, first the velocities were projected in the direction of the plate convergence (i.e., N77°E) and then the model misfit was minimized separately within the six individual subregions (zones 1, 2, 3, 4_5, 6_7 and 8_9 as shown in Figure 7a). To ease the evaluation of the goodness of fit of the models, we display the observed and predicted velocities along the 2-D cross sections in Figure 8. It is important to note that while we constrained the width of the seismogenic zone along the thrust interface directly from the GPS data, we have also adhered to the constraints imposed by the maximum extent of interplate seismicity [*Tichelaar and Ruff*, 1991, 1993].

5. Discussion

[19] Generally, the GPS-derived velocities include (1) transient elastic deformation related to the earthquake cycle, which present a short-term deformation signal compared to geological timescales and (2) long-term permanent plastic deformations that contribute to the formation of tectonic

features, such as mountains, for example. In addition, a small part of the derived velocity vectors is due to observational and processing errors, including local site effects.

[20] Most of the transient deformation can be explained by interseismic, coseismic, and postseismic phases of interplate thrust earthquake cycle [*Thatcher and Rundle*, 1979]. Possible occurrence of slow earthquakes along the plate interface, as recently detected along the Cascadia subduction zone by *Dragert et al.* [2001], can also be characterized as a transient
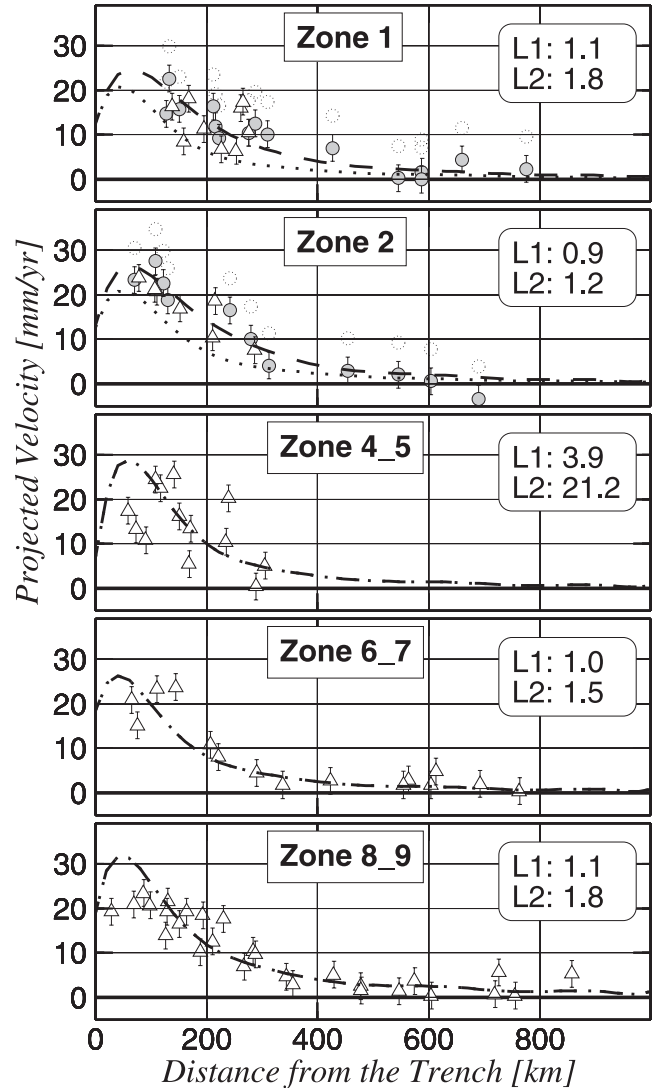
Figure 8. Comparison of the AEDM predictions with observations along the 2-D cross-sectional profiles for the five zones shown in Figure 7a. The data and the model predictions were projected to the plate convergence direction of N77°E. Dotted circles in zones 1 and 2 depict velocities from CAP/SNAPP projects from *Kendrick et al.* [2001]; Filled circles show corrected CAP/SNAPP velocities obtained by subtraction of 7 mm/yr average offset value. See the discussion in section 5.2. Thick dashed and dotted curves represent the predictions of the preferred (North1) and the alternative (North2) AEDM models, respectively (see Figure 7). L_1 and L_2 norms were calculated using equations (1) and (2), respectively. Error bars are given at 1σ level.
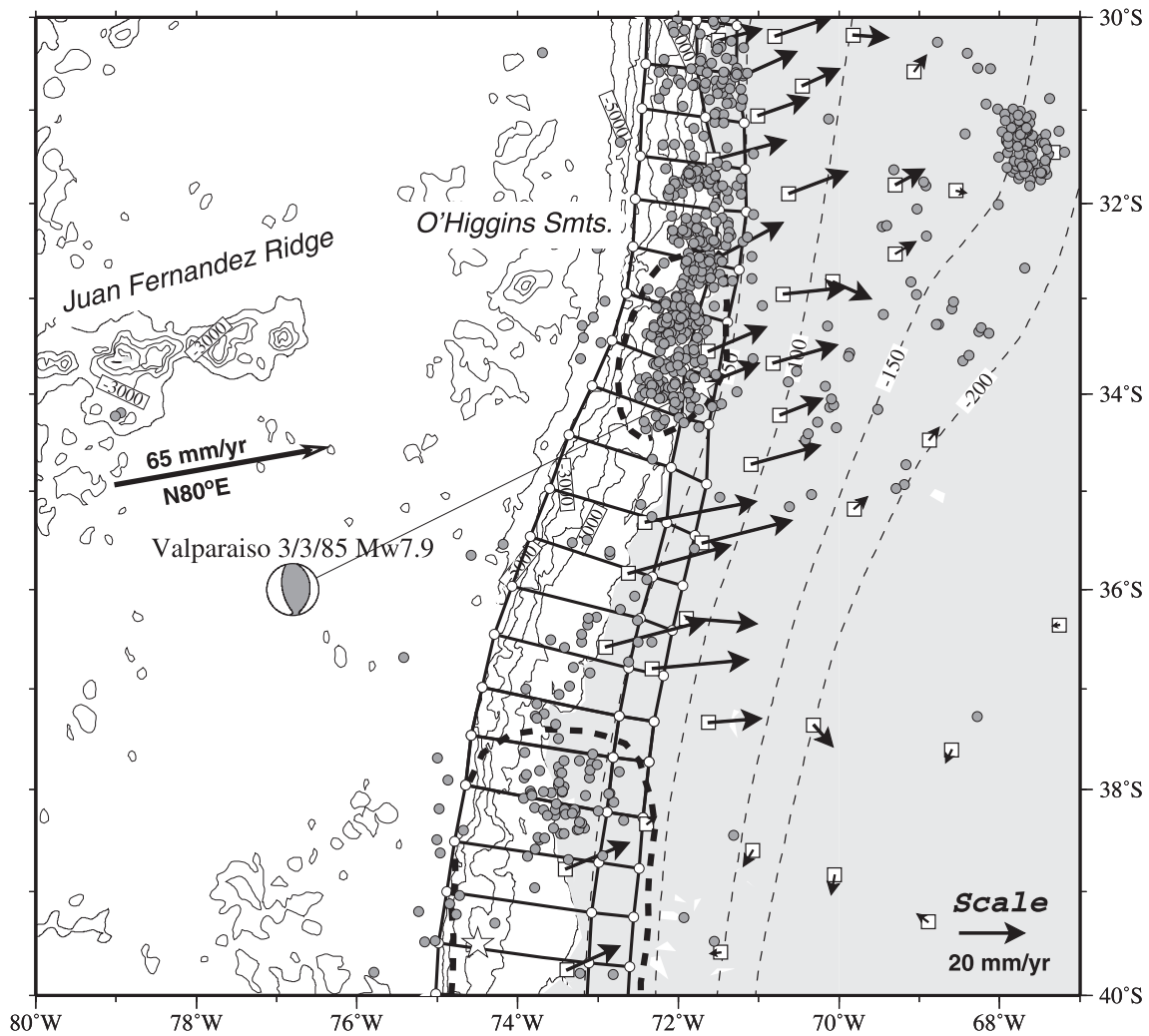
Figure 9. Shallow to deep seismogenic zone transition area. Small circles represent shallow (<70 km) seismicity (1964–1995) from relocated ISC hypocenter data [*Engdahl et al.*, 1998]; Dashed contour lines show the depth of the subducting slab [*Cahill and Isacks*, 1992; *Creager et al.*, 1995]; 1000 m bathymetric contours are from *Smith and Sandwell* [1997]. Plate convergence vector is calculated at 36°S, 77°W based on Euler pole of *Angermann et al.* [1999]. See Figure 1 and 7 captions for additional details.

signal. If the short-term elastic deformation field predicted by the dislocation model is correct, then the residual velocity field, obtained by subtracting the predicted velocities from observations, should represent long-term plastic deformation. The permanent deformation field is mainly visible in the back arc of the subduction but localized, minor deformation might be present within the forearc as well.

[21] In principle, the long-term deformation field consists of components including crustal shortening, block rotations, translation of a forearc sliver and slowly creeping faults. Also, part of the short-term elastic deformation might be transferred into permanent plastic deformation. Depending on the location or the time of measurement, the estimated velocities can be attributed to only some of the above mentioned factors, enabling us to study various processes responsible for present-day crustal deformation.

5.1. Short-Term Deformation Signal

[22] The nature of the observed velocities with vectors oriented parallel to the plate convergence direction and

magnitudes decreasing away from the coast (Figure 2), leads us to the conclusion that the present-day crustal deformation field along the south central Andes is dominated by a short-term transient signal, caused by the locking of the thrust interface between Nazca and South American plates. This type of displacement is characteristic of the interseismic phase of a subduction type earthquake deformation cycle. Similar deformation patterns have been observed with the aid of GPS along other subduction zones around the world: for example, Cascadia [e.g., *Khazaradze et al.*, 1999], Nankai [e.g., *Le Pichon et al.*, 1998], and the Aleutians [e.g., *Freymueller et al.*, 2000].

[23] The dislocation modeling results presented in this paper provide quantitative means of illustrating the dominance of the short-term deformation forces. The two main results that follow from the dislocation model is the requirement of a fully locked thrust interface and a variable depth of coupling along-strike the subduction. The requirement of 100% locking follows from the necessity of imposing a slip on the fault that is equal to the full plate convergence rate in

Table 5. Residual Strain, Rotations, and Translations[a]

No.	$\dot{\epsilon}_1{}^b \pm 1\sigma$	$\dot{\epsilon}_2{}^c \pm 1\sigma$	$\Theta^d \pm 1\sigma$	$\Omega^e \pm 1\sigma$	$C^f \pm 1\sigma$	$C\alpha^g \pm 1\sigma$
1	0.077 ± 0.039	−0.005 ± 0.033	157 ± 4	−0.9 ± 0.3	1.2 ± 0.7	128 ± 34
2	0.015 ± 0.028	−0.020 ± 0.030	123 ± 12	0.7 ± 0.4	0.9 ± 0.7	154 ± 48
4	0.028 ± 0.017	−0.032 ± 0.014	152 ± 3	−1.1 ± 0.2	2.0 ± 0.5	27 ± 15
5	0.000 ± 0.005	−0.004 ± 0.007	133 ± 32	−0.3 ± 0.2	3.7 ± 0.5	105 ± 7
6	0.053 ± 0.024	0.005 ± 0.019	6 ± 3	0.0 ± 0.2	1.7 ± 0.4	33 ± 12
7	0.005 ± 0.009	−0.011 ± 0.008	81 ± 4	0.2 ± 0.1	2.9 ± 0.3	119 ± 7
8	0.029 ± 0.011	−0.020 ± 0.011	141 ± 5	−1.8 ± 0.2	3.5 ± 0.4	111 ± 7
9	0.025 ± 0.013	−0.000 ± 0.012	102 ± 4	−0.0 ± 0.1	2.5 ± 0.4	85 ± 9

[a]Calculations are based on the residual velocities, obtained by subtracting the AEDM-predicted (Figure 7) interseismic velocities from the observations.
[b]Minimum (least compressive) principal strain rate in μstrain/yr.
[c]Maximum (most compressive) principal strain rate in μstrain/yr.
[d]Azimuth of $\dot{\epsilon}_2$ measured clockwise from north.
[e]Rigid body rotation in deg/Myr (positive is clockwise.)
[f]Rigid body translation in mm/yr.
[g]Translation azimuth in degrees from north.

order to match the observed velocities in the forearc. The fact that the thrust interface is fully coupled is significant and it has important implications in terms of the thermo-mechanical and rheological properties of the subduction thrust interface, as well the potential seismic hazard. The fully coupled plate interface is in agreement with the finding of *McCaffrey* [1993, 1994], who suggested that the effective rheology of the forearc in South America is elastic and therefore is less prone to internal deformation and more susceptible to the occurrence of great subduction earth-quakes. Our finding however, is in contrast to the 50% coupling postulated by *Norabuena et al.* [1998] and *Liu et al.* [2000] for the Central Andean margin based on the results from the SNAPP project, just north of our study area. However, the most recent results published by *Bevis et al.* [2001] based on the combined analysis of CAP/SNAPP data suggest 100% coupled interface for this section of the Andean subduction as well.

[24] Regarding the variability of geodetically estimated depth of coupling along-strike the subduction, specifically its increase from ∼35 km depth at 30°S to ∼50 km depth at 36°S latitude: no conventional explanation can be used to explain this phenomenon. For example, following the argument of *Hyndman and Wang* [1993], the observed decrease in the age of the subducting oceanic plate from north to south (that results in a hotter slab) should produce a shallower location of 350°C isotherm along the subduction interface to the south and consequently, should cause a decrease in the locking width, which is exactly opposite to our finding. Another potential factor that could cause the deeper coupled zone, again using the thermal arguments of *Hyndman and Wang* [1993], is a reduced thickness of overlying sediments on top of the oceanic plate, related to the decreased insulating effects. However, in reality what is observed around the latitude 34°S is exactly opposite: here the thickness of sediments increases abruptly from 0.5 km in the north to 2.2 km to the south [*Bangs and Cande*, 1997]. Another possible explanation for a deeper seismo-genic zone could be the subduction of the Juan Fernandez ridge that takes place at the same latitude. The effects associated with the subduction of ridges and seamounts include the creation of asperities and the consequent increase in the amount of seismic coupling along the thrust interface [*Cloos*, 1992; *Scholz and Small*, 1997]. It is not clear however, how the subduction of a ridge no more than

100 km wide could cause the deepening of the seismogenic zone 600 km south of the collision point. The phenomenon might occur from the northward migration of the ridge-trench collision point, but this would require that the orientations of the ridge and the direction of the Nazca plate convergence diverge from each other. However, the present-day plate convergence direction and the orientation of the Juan Fernandez ridge are remarkably parallel (Figure 9). Furthermore, detailed offshore studies of the Juan Fernandez ridge have revealed a significant change in the direction of the ridge (from N80°E to N65°E) occurring near the O'Higgins seamounts [*von Huene et al.*, 1997], implying a southward migration of the ridge. While the latter argument has been used to explain the existence of a flat slab segment between latitudes 28°S and 32°S [e.g., *Cahill and Isacks*, 1992; *Gutscher et al.*, 2000], it also excludes a possibility that subduction of the Juan Fernandez ridge may be responsible for the postulated deepening of the seismogenic zone south of latitude 34°S.

[25] In contrast, we suggest that the increase in the depth of coupling is indeed caused by a reverse process. Specifically, by the steepening of the Nazca plate dip angle below 100 km depth. Although, at this stage we can not provide an exact mechanism that could explain the relationship between the geometry of the slab at deeper depths and the character of coupling in the shallower parts of the plate interface, we suspect that the sea anchor force (F_{sa}) introduced by *Scholz and Campos* [1995] is the most plausible candidate. This force represents a resistance of the subducting slab to the lateral motion through the underlying mantle and mathematically can be represented as

$$F_{sa} = -6\mu\pi \frac{R_h (v_{upn} - v_{rb})}{\lambda} \qquad (3)$$

where μ is viscosity; R_h and λ represent geometric parameters of ellipsoid used to describe the resistance forces associated with the slab translation through the mantle (for detailed description, refer to *Scholz and Campos* [1995]); v_{upn} is the trench-normal velocity of theupper plate; and v_{rb} is the trench roll back velocity. The latter variable is of the main interest to us since it depends on the slab geometry at greater depth through the dipping angle φ:
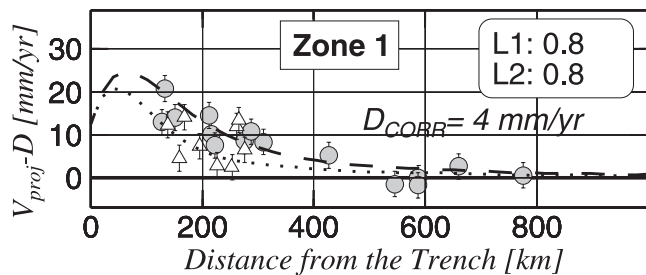
$$v_{rb} = v_v \cot\phi \qquad (4)$$

Figure 10. Crustal shortening related signal. Each network observation was subtracted a constant value (D_{CORR}) to minimize the L_1 norm. CAP/SNAPP data shown as circles also include additional 7 mm/yr correction. Thick dashed and dotted curves represent the predictions of the preferred (North1) and the alternative (North2) AEDM models, respectively (see Figure 7). See Figure 8 caption for further details.

where υ_v is vertical velocity. According to *Scholz and Campos* [1995] seismic decoupling occurs when the normal forces at the plate interface (ΔF_N in equation (5)) decrease below the limit of friction stability transition:

$$\Delta F_N = F_{SA} \sin \psi + F_{SU} \cos \psi \qquad (5)$$

where F_{SU} is a trench suction force; F_{SA} is the slab-pull force and ψ is the slab dip angle at shallower depth. From equations (3), (4), and (5) we can deduce that the increase in the dip angle ϕ reduces the ΔF_N and consequently increases the seismic coupling alongside the thrust interface. This would qualitatively explain the correlation between the observed abrupt steepening of the slab below 100 km depth around latitude 33°S and the suggested increase in the depth of seismogenic zone deduced from AEDM. Naturally, more in-depth analysis will be required to quantify the above hypothesis.

5.2. Long-Term Deformation Signal

[26] Since the inception of GPS measurements in the Andes, the mechanism of crustal shortening, that started in Neogene and presumably continues nowadays, has been almost universally invoked as an additional contributor to the observed velocities. This shortening, mainly driven by the Nazca/SA plate interaction, is believed to be the prime cause for the creation of the Altiplano-Puna plateau [see *Kley and Monaldi*, 1998, and references therein]. The geodetic estimates of the amount of present-day crustal shortening mainly come from observations within the back arc, where the interseismic short-term signal that is dominant along the coast becomes negligible. In the central Andes, between latitudes 12°S and 22°S, this estimate ranges between 9 and 12 mm/yr [*Norabuena et al.*, 1998; *Bevis et al.*, 1999; *Liu et al.*, 2000]. Farther south, lower rates of crustal shortening have been reported: 3.4 mm/yr between 22°S and 26°S [*Klotz et al.*, 1999] and 6 mm/yr between 29°S and 34°S [*Klotz et al.*, 2001].

[27] In this study we utilized two different methods to estimate the amount of possible crustal shortening across the Andes. The first method is based on the assumption that the present-day crustal shortening is solely due to the

shifting of the Brazilian shield toward the trench. This would indeed mean that the velocities presented in the reference frame fixed to the Brazilian shield (i.e., stable SA continent), will also include a contribution due to the crustal shortening. To test this hypothesis, for the five individual sections shown in Figure 8, we have searched for the best values of the correction factors in increments of 1 mm/yr, to ensure the minimum value of L_1 norm (Table 6). For the northernmost two zones however, where a serious discrepancy exists between our data and the velocities estimated by *Kendrick et al.* [2001] for the CAP [*Bevis et al.*, 1999] and SNAPP [*Norabuena et al.*, 1998] data, we had to perform additional steps to make the two data sets compatible. Specifically, first we selected five pairs of SAGA and CAP/SNAPP stations that were located closest
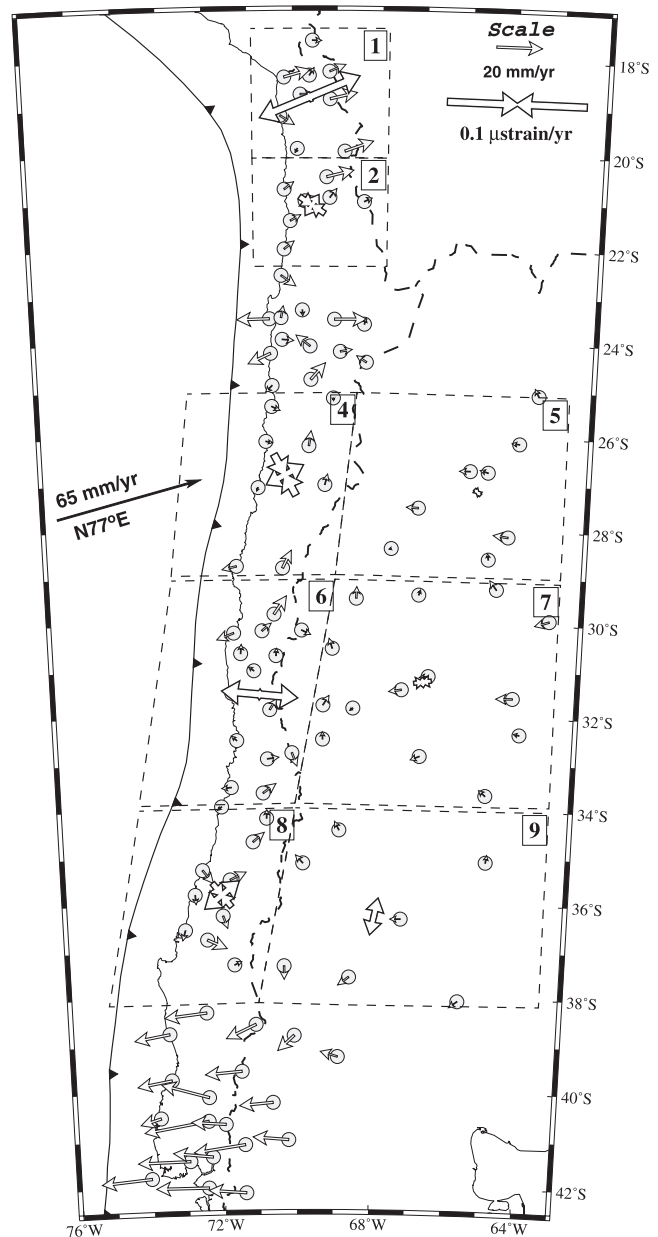

Figure 11. Strain rates deduced from residual velocity field. Numerical results are given in Table 5. See Table 3 and the caption of Figure 5 for further explanations.

Table 6. L_1 Norm Misfits for the Preferred Model[a]

Zone	SAGA	C/S[b]	C/S_{CORR}[c]	All[d]
1	1.5	3.0	0.8	1.1
2	0.7	2.7	1.0	0.9
4_5	1.0	–	–	1.0
6_7	1.1	–	–	1.1
8_9	1.1	–	–	1.1
		Corrected for Crustal Shortening[e]		
1	0.8	–	0.7	0.8

[a]L_1 (in mm/yr) was calculated using equation (1). Zone locations are shown in Figure 7.

[b]Original CAP/SNAPP data from *Kendrick et al.* [2001].

[c]CAP/SNAPP data corrected by 7 mm/yr in the direction of N77°E.

[d]Using SAGA and C/S_{CORR} values.

[e]Obtained by subtracting D_{CORR} correction value given in Figure 10.

to each other (shown with dashed circles and identified with four-letter station names in Figure 3). Second, we estimated an average offset between their velocities, which was ~7 mm/yr in the plate convergence direction of N77°E. Finally, we subtracted this value from the CAP/SNAPP data and searched for the best value of the correction factor that could account for the suspected crustal shortening. The only significant reduction in the L_1 norm we were able to achieve was for the northernmost zone 1, where the amount of required crustal shortening equals 4 mm/yr (D_{CORR} in Figure 10). For the rest of the zones, no statistically significant reduction in L_1 norm could be achieved. The fact that only zone 1 along the entire stretch of the study area included the possibility of the crustal shortening related signal, suggests the existence of a different deformation mechanism in this area. Most likely related to abrupt change in the strike of the subduction at the Arica bend, or a change in the dip angle of the slab, or a change in the width of the locked zone. The actual amount of the shortening suggested by us however, can be subject to discussion, since this value directly depends on the parameters used in the AEDM. In our opinion, the suggested 4 mm/yr shortening rate, represents a lower limit, since it is calculated for the preferred model (North1), where the subduction interface is fully locked and extends to its maximum depth of 55 km, thus predicting the highest possible interseismic velocities. If we had considered the alternative model with significantly shallower depth of geodetic coupling (North2 in Figure 7), than the amount of possible shortening would have increased to 6–7 mm/yr. The value that is closer to the

earlier reported crustal shortening rates of 9–12 mm/yr [*Norabuena et al.*, 1998; *Bevis et al.*, 1999; *Liu et al.*, 2000]. In the future we believe, this parameter can be resolved with higher confidence by conducting a nonlinear inversion to estimate simultaneously the long-term and short-term deformation rates, based on the combined analysis of the SAGA, CAP, and SNAPP data sets.

[28] The second method we used to investigate possible long-term deformation signal in the GPS measurements included the examination of the longitudinal and latitudinal dependence of E-W and N-S components of the residual velocity field, respectively. From eight zones shown in Figure 11, only two zones, located alongside each other between latitudes 29°S and 34°S, showed any significant internal deformation at 95% confidence level (Table 5). These included the suggestion of the continued E-W compression within the back arc in zone 7, based on the existence of a negative slope of -0.011 ± 0.003 µstrain/yr (Figure 12). This corresponds to ~6 mm/yr shortening across the 600 km distance, which falls within the range of 2–7 mm/yr shortening rate estimated from geological observations spanning the last 25 Ma [*Kley and Monaldi*, 1998]. The second significant observation included the indication of a trench-perpendicular (E-W) extension within the forearc in zone 6. The strain rate derived from the least squares fit to the E-W residual velocity component equals to 0.051 ± 0.016 µstrain/yr (Figure 12). Interestingly, the recent geotectonic field studies conducted within the same area, between latitudes 30°S and 31°S, reveal the evidence for N-S striking Quaternary normal faulting, indicating E-W extension [*Heinze et al.*, 2001].

[29] Until now we have ignored the presence of the buoyancy forces due to variations in the crustal thickness and the topography [*Molnar and Lyon-Caen*, 1988; *Wdowinski and O'Connell*, 1991]. As mentioned earlier, north of 30°S the Andes are characterized by the presence of high topography that forms the Altiplano/Puna plateau. This excess mass imposes significant extensional forces directed away from the topographic highs. As a result, in the forearc, the tectonic and the buoyancy forces would be oriented opposite to each other, causing the decrease in the observed velocity vectors and consequently would lead to the shallower seismogenic zone deduced from the dislocation modeling. In the south however, the observed velocities would be higher, because with the more subdued topography (Figure 2) the trenchward oriented buoyancy forces would be missing. This could indeed be the alternative
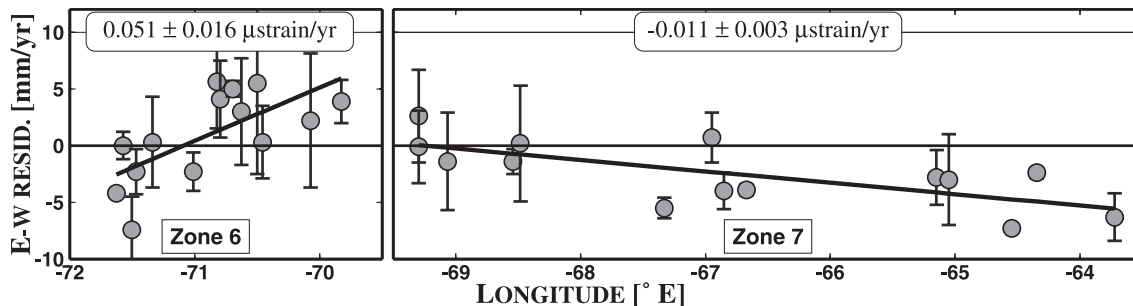

Figure 12. Long-term deformation signal in the residual velocities. Significant trends at 95% confidence level were found only within zones 6 and 7. Uncertainties are given at 1σ level.

explanation for the postulated deepening of the coupling zone south of latitude 34°S. However, it is not clear that one could detect the deformation caused by this type of gravitational buoyancy forces during the short observation period of GPS campaigns. For example, on the basis of 3-D finite element viscoelastic modeling results, *Liu et al.* [2000] suggest that the effects of the buoyancy forces on the surface deformation become significant only on longer geological timescales (>10^6 years).

6. Conclusions

[30] From four GPS campaigns conducted between 1994 and 1997 we estimated the present-day crustal deformation field along the Andes, between latitudes 17°S and 45°S. On the basis of three-dimensional dislocation modeling results, we conclude that the majority of the observed velocities represent the short-term transient signal related to various phases of the earthquake deformation cycle. Specifically, in the central part of the study area (between latitudes 26°S and 38°S) the deformation field is dominated by the interseismic signal, caused by 100% locking of the thrust interface between Nazca and South American plates. The depth extent of locking is not uniform along-strike the subduction but increases from north to south, exhibiting positive correlation with the steeply dipping portions of the slab.

[31] In addition to the short-term, transient signal the GPS derived velocities also include long-term deformation signal. Such as, an evidence for the continuing crustal shortening in the northern part of the study area, as well as, an indication for a regional E-W extension in the forearc, between latitudes 25°S and 30°S, in agreement with the recent geotectonic studies.

References

Angermann, D., G. Baustert, R. Galas, and S. Y. Zhu, EPOS.P.V3 (Earth Parameter & Orbit System): Software User Manual for GPS Data Processing, *Tech. Rep. STR97/14*, GeoForschungsZentrum, Potsdam, Germany, 1997.

Angermann, D., J. Klotz, and C. Reigber, Space-geodetic estimation of the Nazca-South America Euler vector, *Earth Planet. Sci. Lett.*, *171*, 329–334, 1999.

Bangs, N. L., and S. C. Cande, Episodic development of a convergent margin inferred from structures and processes along the southern Chile margin, *Tectonics*, *16*, 489–503, 1997.

Barrientos, S. E., Slip distribution of the 1985 central Chile earthquake, *Tectonophysics*, *145*, 225–241, 1988.

Beutler, G., M. Rothacher, S. Schaer, T. A. Springer, J. Kouba, and R. E. Neilan, The International GPS Service (IGS); an interdisciplinary service in support of Earth sciences, *Adv. Space Res.*, *23*, 631–653, 1999.

Bevis, M., E. C. Kendrick, R. J. Smalley, T. Herring, J. Godoy, and F. Galban, Crustal motion north and south of the Arica deflection; comparing recent geodetic results from the central Andes, *Geochem. Geophys. Geosyst.*, *1*, Paper number 1999GC000011, 1999.

Bevis, M., E. Kendrick, R. J. Smalley, B. A. Brooks, R. W. Allmendinger, and B. L. Isacks, On the strength of interplate coupling and the rate of back arc convergence in the central Andes: An analysis of the interseismic velocity field, *Geochem. Geophys. Geosyst.*, *3*, doi:10.129/2001GC000198, 2001.

Cahill, T., and B. L. Isacks, Seismicity and shape of the subducted Nazca plate, *J. Geophys. Res.*, *97*, 17,503–17,529, 1992.

Cifuentes, I. L., The 1960 Chilean earthquakes, *J. Geophys. Res.*, *94*, 665–680, 1989.

Cloos, M., Thrust-type subduction-zone earthquakes and seamount asperities: A physical model for seismic rupture, *Geology*, *20*, 601–604, 1992.

Creager, K. C., C. Ling Yun, J. P. Winchester, and E. R. Engdahl, Membrane strain rates in the subducting plate beneath South America, *Geophys. Res. Lett.*, *22*, 2321–2324, 1995.

DeMets, C., R. G. Gordon, D. F. Argus, and S. Stein, Current plate motions, *Geophys. J. Int.*, *101*, 425–478, 1990.

DeMets, C., R. G. Gordon, D. F. Argus, and S. Stein, Effect of recent revisions to the geomagnetic reversal time scale on estimates of current plate motions, *Geophys. Res. Lett.*, *21*, 2191–2194, 1994.

Dixon, T. H., An introduction to the Global Positioning System and some geological applications, *Rev. Geophys.*, *29*, 249–276, 1991.

Dragert, H., K. Wang, and T. James, A silent slip event on the deeper Cascadia subduction interface, *Science*, *292*, 1525–1528, 2001.

Engdahl, E. R., R. Van der Hilst, and R. Buland, Global teleseismic earthquake relocation with improved travel times and procedures for depth determination, *Bull. Seismol. Soc. Am.*, *88*, 722–743, 1998.

Flück, P., R. D. Hyndman, and K. Wang, Three-dimensional dislocation model for great earthquakes of the Cascadia subduction zone, *J. Geophys. Res.*, *102*, 20,539–20,550, 1997.

Freymueller, J. T., S. C. Cohen, and H. J. Fletcher, Spatial variations in present-day deformation, Kenai Peninsula, Alaska, and their implications, *J. Geophys. Res.*, *105*, 8079–8101, 2000.

Gutscher, M. A., W. Spakman, H. Bijwaard, and E. R. Engdahl, Geodynamics of flat subduction: Seismicity and tomographic constraints from the Andean margin, *Tectonics*, *19*, 814–833, 2000.

Heinze, B., G. Michel, and G. Khazaradze, Active intra-plate faulting in the Chilean forearc near La Serena (30°–31°S): Evidence from neotectonic and GPS data, in *2001 Margins Meeting*, edited by S. Roth, and A. Rueggeberg, *Dtsch. Geol. Ges.*, *14*, 87–88, 2001.

Hyndman, R. D., and K. Wang, Thermal constraints on the zone of major thrust earthquake failure: The Cascadia subduction zone, *J. Geophys. Res.*, *98*, 2039–2060, 1993.

Hyndman, R. D., M. Yamano, and D. A. Oleskevich, The seismogenic zone of subduction thrust faults, *Island Arc*, *6*, 244–260, 1997.

Jordan, T. E., B. L. Isacks, R. W. Allmendinger, J. A. Brewer, V. A. Ramos, and C. J. Ando, Andean tectonics related to geometry of subducted Nazca Plate, *Geol. Soc. Am. Bull.*, *94*, 341–361, 1983.

Kendrick, E., M. Bevis, R. J. Smalley, and B. A. Brooks, An integrated crustal velocity field for the central Andes, *Geochem. Geophys. Geosyst.*, *2*, Paper number 10.1029/2001GC000191, 2001.

Khazaradze, G., Tectonic deformation in western Washington State from Global Positioning System measurements, Ph.D. thesis, Univ. of Wash., Seattle, 1999.

Khazaradze, G., A. Qamar, and H. Dragert, Tectonic deformation in western Washington from continuous GPS measurements, *Geophys. Res. Lett.*, *26*, 3153–3156, 1999.

Khazaradze, G., K. Wang, J. Klotz, Y. Hu, and J. He, Prolonged postseismic deformation of the 1960 great Chile earthquake and implications for mantle rheology, *Geophys. Res. Lett.*, *29*, 2002.

Kley, J., and C. R. Monaldi, Tectonic shortening and crustal thickness in the central Andes: How good is the correlation?, *Geology*, *26*, 723–726, 1998.

Klotz, J., et al., GPS-derived deformation of the central Andes including the 1995 Antofagasta M_w = 8.0 earthquake, *Pure Appl. Geophys.*, *154*, 3709–3730, 1999.

Klotz, J., G. Khazaradze, D. Angermann, C. Reigber, R. Perdomo, and O. Cifuentes, Earthquake cycle dominates contemporary crustal deformation in central and southern Andes, *Earth Planet. Sci. Lett.*, *193*, 437–446, 2001.

Le Pichon, X., S. Mazzotti, P. Henry, and M. Hashimoto, Deformation of the Japanese Islands and seismic coupling: An interpretation based on GSI permanent GPS observations, *Geophys. J. Int.*, *134*, 501–514, 1998.

Liu, M., Y. Yang, S. Stein, Y. Zhu, and J. Engeln, Crustal shortening in the Andes: Why do GPS rates differ from geological rates?, *Geophys. Res. Lett.*, *27*, 3005–3008, 2000.

McCaffrey, R., On the role of the upper plate in great subduction zone earthquakes, *J. Geophys. Res.*, *98*, 11,953–11,966, 1993.

McCaffrey, R., Global variability in subduction thrust zone-forearc systems, *Pure Appl. Geophys.*, *142*, 173–224, 1994.

Molnar, P., and H. Lyon-Caen, Some simple physical aspects of the support, structure, and evolution of mountain belts, *Spec. Pap. Geol. Soc. Am.*, *218*, 179–207, 1988.

Norabuena, E., L. Leffler-Griffin, A. Mao, T. Dixon, S. Stein, S. I. Sacks, L. Ocola, and M. Ellis, Space geodetic observations of Nazca-South America convergence across the central Andes, *Science*, *279*, 358–362, 1998.

Norabuena, E., T. Dixon, S. Stein, and C. G. A. Harrison, Decelerating Nazca-South America and Nazca-Pacific Plate motion, *Geophys. Res. Lett.*, *26*, 3405–3408, 1999.

Okada, Y., Internal deformation due to shear and tensile faults in a half-space, *Bull. Seismol. Soc. Am.*, *82*, 1018–1040, 1992.

Oleskevich, D. A., R. D. Hyndman, and K. Wang, The updip and downdip limits to great subduction earthquakes: Thermal and structural models of Cascadia, south Alaska, SW Japan, and Chile, *J. Geophys. Res.*, *104*, 14,965–14,992, 1999.

Pacheco, J. F., L. R. Sykes, and C. H. Scholz, Nature of seismic coupling along simple plate boundaries of the subduction type, *J. Geophys. Res.*, *98*, 14,133–14,159, 1993.

Plafker, G., and J. C. Savage, Mechanism of the Chilean earthquakes of May 21 and 22, 960, *Geol. Soc. Am. Bull.*, *81*, 1001–1030, 1970.

Ruegg, J. C., et al., The M_w8.1 Antofagasta (north Chile) earthquake of July 30, 1995: First results from teleseismic and geodetic data, *J. Geophys. Res.*, *23*, 917–920, 1996.

Scholz, C. H., and J. Campos, On the mechanism of seismic decoupling and back arc spreading at subduction zones, *J. Geophys. Res.*, *100*, 22,103–22,115, 1995.

Scholz, C. H., and C. Small, The effect of seamount subduction on seismic coupling, *Geology*, *25*, 487–490, 1997.

Sillard, P., Z. Altamini, and C. Boucher, The ITRF96 realization and its associated field, *Geophys. Res. Lett.*, *25*, 3223–3226, 1998.

Simkin, T., and L. Siebert, *Volcanoes of the World*, 2nd ed., Geosci. Press, Tucson, Ariz., 1994.

Smith, W. H. F., and D. T. Sandwell, Global sea floor topography from satellite altimetry and ship depth soundings, *Science*, *277*, 1956–1962, 1997.

Thatcher, W., and J. B. Rundle, A model for the earthquake cycle in underthrust zones, *J. Geophys. Res.*, *84*, 5540–5556, 1979.

Tichelaar, B. W., and L. J. Ruff, Seismic coupling along the Chilean subduction zone, *J. Geophys. Res.*, *96*, 11,997–12,022, 1991.

Tichelaar, B. W., and L. J. Ruff, Depth of seismic coupling along subduction zones, *J. Geophys. Res.*, *98*, 2017–2037, 1993.

von Huene, R., J. Corvalan, E. R. Flueh, K. Hinz, J. Korstgard, C. R. Ranero, and W. Weinrebe, Tectonic control of the subducting Juan Fernandez Ridge on the Andean margin near Valparaiso, Chile, *Tectonics*, *16*, 474–488, 1997.

Wang, K., J. He, H. Dragert, and T. James, Three-dimensional viscoelastic interseismic deformation model for the Cascadia subduction zone, *Earth Planets Space*, *53*, 295–306, 2001.

Wdowinski, S., and R. J. O'Connell, Deformation of the central Andes (15°–27°S) derived from a flow model of subduction zones, *J. Geophys. Res.*, *96*, 12,245–12,255, 1991.

Whitman, D., B. L. Isacks, and S. M. Kay, Lithospheric structure and along-strike segmentation of the Central Andean Plateau: Seismic Q, magmatism, flexure, topography and tectonics, *Tectonophysics*, *259*, 29–40, 1996.

———————————

G. Khazaradze, Universitat de Barcelona, Departament de Geodinàmica i Geofisica, 08028 Barcelona, Spain. (kgiorgi@geo.ub.es)

J. Klotz, GeoForschungsZentrum Potsdam, Telegrafenberg, D-14473 Potsdam, Germany. (klotz@gfz-potsdam.de)